Journal of Solid State Chemistry 315 (2022) 123462

Contents lists available at ScienceDirect

Journal of Solid State Chemistry

journal homepage: www.elsevier.com/locate/jssc

Unexpected wide tuning of ferroelectric properties by varying the Er concentration in $La_{2-x}Er_x(MoO_4)_3$ (x = 0.75, 1, 1.25) solid solutions

G. Gil-de-Cos [a,*], M.E. Torres [a,b], C. González-Silgo [a,b], K. Soler-Carracedo [a], I.R. Martín [a,b], F. Rivera-López [c], S. Rodríguez-Rodríguez [c]

[a] Departamento de Física, Universidad de La Laguna, Apdo 456, E-38200 San Cristóbal de La Laguna, Santa Cruz de Tenerife, Spain
[b] Instituto Universitario de Materiales y Nanotecnología IMN, Universidad de La Laguna, La Laguna, Tenerife, 38200, Spain
[c] Departamento de Ingeniería Industrial, Escuela Superior de Ingeniería y Tecnología, Universidad de La Laguna, Apdo 456, E-38200 San Cristóbal de La Laguna, Santa Cruz de Tenerife, Spain

ARTICLE INFO

Keywords:
Inorganic compounds
Crystal structure
Dielectric properties
Ferroelectricity
Phase transitions

ABSTRACT

Powder samples of the series $La_{2-x}Er_x(MoO_4)_3$ (x = 0.75, 1, 1.25) were prepared by solid-state reaction from the La and Er trimolybdates. The correlation of the ferroelectric properties with the crystal structure, as a function of the x concentration, was studied by X-ray diffraction (XRD), dielectric and optical spectroscopy, and the ferroelectric hysteresis loop measurements. The β′-$Gd_2(MoO_4)_3$ structure type was identified by a non-conventional Rietveld method, including a symmetry analysis. Contrary to the expectations, the ferroelectric properties were intensified by the Er^{3+} concentration increase: the maximum polarization for x = 1.25 reaches one order of magnitude larger than that of x = 0.75, and the Curie temperature increase was around 200 K. This unexpected behavior is opposite of that observed for the improper ferroelectrics $RE_2(MoO_4)_3$, where the ferroelectric properties are enhanced with the RE ionic radius increase. Hence, the series $La_{2-x}Er_x(MoO_4)_3$ show an "wider tuning range" for ferroelectric properties opposite to the rare earth trimolybdate family.

1. Introduction

Luminescent double oxides and oxysalts containing rare-earth ions have attracted much interest as they are great candidates for many applications, as in LEDs [1–3], solid-state lasers [4,5], display devices (biological labeling) [6], sensors (optical thermometers) [7] and photocatalysis (solar cells) [8,9]. Among them, rare-earth compounds with formula $RE_2(MO_4)_3$ (M ≡ W, Mo and RE is the rare-earth cation) have been widely studied due to their longevity, low cost, low toxicity, and thermal and photochemical stability [10–13]. Moreover, their luminescent properties can be easily varied by adjusting the concentration and type of rare-earth via solid solution or doping [14–17].

Gadolinium molybdate is the most representative crystal of this family. Its interest lies in the fact that it has a phase whose structural type, called β′-$Gd_2(MoO_4)_3$, is ferroelectric and ferroelastic [18]. Trimolybdates showing this phase are those with RE ≡ Pr – Ho and Y and solid solutions [19–21]. The polar symmetry also makes them possible to be pyroelectric and piezoelectric [22]. In addition, they exhibit non-linear optical phenomena such as second harmonic generation (SHG) and Raman amplification [23], allowing more compact lasers, for instance. Doped crystals also exhibit multiphoton absorption and up-conversion processes [24]. More recently, attention has also been paid to the coupling of ferroelectric and ferroelastic arrangements in $Gd_2(MoO_4)_3$ thin films for their applicability in electronic devices [25,26].

The β′-phase is also distinguished by the fact that it is one of the most studied improper ferroelectric, where a secondary order parameter (in the Landau phenomenological theory) is responsible for the spontaneous polarization and deformation [27,28]. The paraelectric phase (β-phase) belongs to the non-polar space group $P\bar{4}2_1m$, stable above 433 K. Its crystal structure also consists of Gd^{3+} ions surrounded by $[MoO_4]^{2-}$ tetrahedra [29,30]. After the condensation of a non-polar unstable primary phononic mode [associated with the M-point (1/2,1/2,0) at the edge of the Brillouin zone], which manifests itself as cooperative rotations of the $[MoO_4]^{2-}$ tetrahedra, the structure is reduced to the orthorhombic space group *Pba2* (β′-phase). Then, the unit cell is doubled (with the transformation: *a*-*b*, *a* + *b*, *c*; 0, ½, 0). Another symmetry mode (in the center of the Brillouin zone) is allowed and has a secondary character as it only breaks the symmetry up to the intermediate subgroup *Cmm2* [31] and is coupled with the previous one. This secondary mode, with polar

* Corresponding author.
E-mail addresses: alu0100235@ull.edu.es, ggildecos@gmail.com (G. Gil-de-Cos).

https://doi.org/10.1016/j.jssc.2022.123462
Received 15 June 2022; Received in revised form 25 July 2022; Accepted 29 July 2022
Available online 12 August 2022

symmetry, is responsible for the spontaneous polarization P_s (and the spontaneous deformation ε_s) along the *c-axis* in the β′-phase, and it is caused by the antiparallel displacements of the Gd^{3+} cations and $[MoO_4]^{2-}$ anions in that direction. These motions are mostly cancelled. Therefore, the spontaneous polarization ($P_s = 0.2$ μC/cm^2) reaches values one order of magnitude smaller than in most of proper ferroelectrics, where the polarization is the primary phononic mode (primary order parameter) [30–32].

However, one of the main consequences of the second-order nature of the spontaneous polarization is the dielectric irregularities appearing in the improper ferroelectrics, making them considerably different from the proper ones. In particular, the thermal dependence of the permittivity does not follow the Curie-Weiss law, and an intensive electric field does not suppress the phase transition [28,33]. These anomalies allow working over a wide temperature range where the dielectric permittivity is stable. Thus, the induced polarization results from the pyroelectric (or piezoelectric) effect, not from the variation of the electrical permittivity [33–35]. In the case of rare-earth trimolybdates, the theory developed for the improper ferroelectrics agrees quantitatively with the experiments [18,36]. Improper ferroelectrics are also being investigated for their potential as pyroelectric energy harvesters [37] and their electrocaloric effect [38].

On the other hand, the advantage of the "lanthanide shrinkage" may be used for suitable replacements. When gadolinium is substituted by other chemical elements of larger (or smaller) ionic radius in the ferroelectric phase, the oxygen atoms move away from (or closer to) the middle position of the paraelectric structure. Thus, Pr – Eu (or Tb – Ho) trimolybdates need more (or less) vibrational energy to reach the transition temperature. Their transition temperatures are highest: 508 K–434 K (or lowest: 433 K–394 K) [28], according to the increase (or decrease) of the volume and the spontaneous polarization and the cell parameters expand less (or more) isotropically [19,20]. However, this "chemical pressure" does not have the same behavior as the thermal or hydrostatic contraction, where the decrease of the unit cell volume may increase the spontaneous polarization, and the *a* and *b cell* parameters are contracted anisotropically, while the *c* parameter increases when the temperature decreases [39–41].

The interest in controlling the ferroelectricity and related properties, and the luminescence in these compounds has encouraged the study of solid solutions where different RE atoms are substituted. In this sense, it must be taken into account that the β′-phase is not the most stable under ambient conditions, except for $Ho_2(MoO_4)_3$ and $Y_2(MoO_4)_3$. The most stable crystal structure for trimolybdates with RE ≡ La – Nd is the $La_2(MoO_4)_3$ polytype. When RE ≡ Sm – Dy, the α-phase [with the α-$Eu_2(WO_4)_3$ structural polytype] is more stable; both phases are called modulated scheelites [42]. In addition, the heavier rare-earth trimolybdates crystallize in the hydrated γ-$Sc_2(WO_4)_3$ phase with negative thermal expansion [43,44]. The preparation of these compounds can be complicated because mixtures of different polymorphous can arise, depending on the preparation conditions and the lanthanide radius. It is easy to synthesize the β′-phase from isostructural rare-earth trimolybdates; however, it is also possible to obtain it from non-isostructural end compounds. For example, solid solution families of trimolybdates have been studied with interesting results for luminescent and/or ferroelectric properties: $RE_{2-x}Eu_x(MoO_4)_3$ (RE = Gd, Sm) [45,46], $Y_{2-x}Eu_x(MoO_4)_3$ [47], $Lu_{2-x}Eu_x(MoO_4)_3$ [48], $Lu_{2-x}Gd_x(MoO_4)_3$ [49], $Gd_{2-x}Bi_x(MoO_4)_3$ [50], $Gd_{2-x}Yb_{2x}(MoO_4)_3$ [51,52] and $Gd_{2(1-x)}Eu_{2x}(Mo_yW_{1-y}O_4)_3$ [53]. It should be recalled that the tungstate family with the formula $RE_2(WO_4)_3$ never exhibit the β′-phase, neither when they are compressed under high pressure [41,54].

In this work, we are interested in the $La_{2-x}Er_x(MoO_4)_3$ solid solution, where the intermediate compound (x = 1) is the most investigated and for which researchers have studied the ferroelectric-paraelectric transition [55,56] and the up-conversion luminescence independently [57–59]. We will characterize its dielectric and ferroelectric properties as a function of the x concentration, concerning the crystalline expansion or compression and taking advantage of the Er^{3+} luminescence. This family of compounds attracts strong attention and interest because they are both multiferroic and luminescent.

2. Experimental

2.1. Synthesis

The $La_{2-x}Er_x(MoO_4)_3$ system, with x = 0.75, 1, and 1.25, was obtained from the α-$La_2(MoO_4)_3$ and γ-$Er_2(MoO_4)_3$ phases, which were synthesized by solid-state reaction. The phases were synthesized from La_2O_3 and MoO_3 oxides, and Er_2O_3 and MoO_3 oxides (Aldrich, 99.99%), respectively. Before the stoichiometric mixing of the corresponding oxides, they were precalcined for 10 h at 923 K (MoO_3) and 1173 K (La_2O_3 and Er_2O_3). The oxides were mixed and the powder was homogenized by grinding in an agate mortar for at least 1 h, and, then, the samples were compacted in a uniaxial hydraulic press at a pressure of 230 MPa. Finally, the resulting pellets were sintered at 1073 K for 48 h to obtain α-$La_2(MoO_4)_3$ and at 1323 K for 48 h to obtain γ-$Er_2(MoO_4)_3$.

Once the aforementioned pure phases were obtained, solid solutions were synthesized by mixing and homogenizing the powder of the end trimolybdates for the three concentrations. The hydrated and dehydrated $Er_2(MoO_4)_3$ phases were weighted to ensure the desired stoichiometry. Two heat treatments were applied to $La_{0.75}Er_{1.25}(MoO_4)_3$, with intermediate milling and compaction at 230 MPa of the corresponding powder, at 1073 K and 1173 K for 24 h each, followed by a subsequent quenching to 473 K. The $LaEr(MoO_4)_3$ and $La_{1.25}Er_{0.75}(MoO_4)_3$ samples were subjected to a single heat treatment at 1173 K for 48 h and at 1173 K for 36 h, respectively, and a subsequent quenching to 473 K.

2.2. Characterization techniques

X-ray powder diffraction (XRD) was used to monitor the phase purity and refine crystal structure. Diffractograms were collected using a Panalytical Empyrean diffractometer with Cu-Kα radiation [wavelength: $\lambda(Cu\text{-}K\alpha_1) = 1.54056$ Å and $\lambda(Cu\text{-}K\alpha_2) = 1.54443$ Å] passing through a Ni filter, a fixed divergence slit of 1/2° and a receiving slit of 1/8°. Measurements were collected at an angular interval of $5° < 2\theta < 120°$ with a step of 0.02° and 57 s step time [60].

An SDT650 Simultaneous Thermal Analyzer (TA Instruments) was used to study the thermal stability and detect the paraelectric-ferroelectric phase transition temperatures. Simultaneous thermogravimetric analysis (TG/DTG) and differential scanning calorimetry (DSC) were carried out in an inert atmosphere, with continuous nitrogen flow and heating and cooling ramps of 2, 5, and 10 K/min in a temperature range of the cyclic process between 300 and 1173 K [61].

The emission spectra as a function of temperature were obtained. The sample was placed in the center of a tubular furnace with the temperature control by a type K thermocouple. The sample was excited with a continuum laser at 457 nm from one side of the furnace. On the other side of the furnace, the emission coming from the sample was collected with a convex lens and focused in an optical fiber coupled to a 0.3 m single grating spectrometer (*Andor SR-3031-B*) equipped with a cooled CCD detector (*Newton DU920 N*). All the spectra were corrected from the instrument response.

The dielectric permittivity and conductivity study was carried out in a frequency range from 5 Hz to 13 MHz applying an alternating voltage with a peak value of 1.1 V and in a temperature range from 313 K to 913 K, employing an *HP* 4192A LF *Impedance Analyzer*. This characterization was performed on 13 mm diameter pellets with thicknesses of 0.6 mm and whose surfaces were coated with platinum dye (*6082-Platinum paste - Metalor*).

The Polarization-Electric Field ferroelectric hysteresis loop (P-E curve) measurement was performed by applying a triangular signal with a maximum amplitude of 1900 V and a period between 20 and 30 ms. These cycles were recorded on pellets, with electrodes (Pt) and at room

temperature. In this case, the used equipment was a *Precision LC Main Unit* with a *High Voltage Precision* 10 kV *HVI-SC interface* from *Radiant Technologies, Inc.* [62].

2.3. Data analysis

2.3.1. Crystal data refinement

Rietveld refinement was performed with the use of the Fullprof software [63] for each compound, for the diffractograms collected at room temperature. All compounds were identified and refined in reference to the ferroelectric β′-$Gd_2(MoO_4)_3$ phase. For the compound with x = 0.75, small impurities of $La_2(MoO_4)_3$ were observed, and this phase was added to the refinement. The Thompson-Cox-Hasting pseudo-Voigt profile shape function modeled the experimental profiles, and the background was modeled by interpolating several selected points. The crystal structure analysis is also based on conventional powder X-ray diffraction data where oxygen scattering is relatively insensitive in the presence of heavy rare earth and molybdenum ions, and hence the determination of its position is less feasible. A suitable way to solve the problem is to refine the displacements from the paraelectric phase "ferroelectric distortion" instead of the atomic coordinates. The ferroelectric structures were obtained, analyzing the distortion from the paraelectric phase. The AMPLIMODES software, from the Bilbao Crystallographic Server, relates the two structures based on symmetry-adapted modes and calculates the amplitudes and polarization vectors of the distortion modes of different symmetry frozen in the less symmetrical structure [64]. The spontaneous polarization can be closely related to the amplitude of some symmetry lowering mode [65]. The "ferroelectric distortion" in these compounds was decomposed into three symmetry modes [31]: 1) a primary mode corresponds to the irreducible representation M_2+M_4 associated with the point M (1/2, 1/2, 0) on the boundary of the Brillouin zone. 2) A secondary polar mode in the center of the Brillouin zone with the symmetry given by the irreducible representation Γ_3. 3) Finally, another secondary mode given by the irreducible representation Γ_1 maintains the symmetry of the prototype phase. Some of the amplitudes of these symmetry modes were canceled, which would help to reduce the number of refined parameters. This refinement has many advantages, especially in the present case, where the distortions are caused by oxygen displacements with very small X-ray scattering amplitude. To obtain a prototype paraelectric structure (the theoretical β-phase), necessary to refine the experimental ferroelectric phase distortions, we start from the data of the ferroelectric phase (theoretical β′-phase) of $LaEr(MoO_4)_3$ compound, theoretically calculated by the *ab initio* density-functional-theory (DFT) method, with a cell volume of 1200 $Å^3$ in a previous study [56]. Since in the paraelectric phase there is only one site for the rare-earth atom in the asymmetric unit, it is not possible to calculate a theoretical structure with fractional occupancy factors of the La and Er atoms. Then, we calculated this more symmetric phase from the β′-phase with the PSEUDO software [66]. The reliability of our experimental results can be verified with the results of these theoretical calculations, which are also shown in the tables. Thus, the so-called "amplimodes" (amplitudes of the symmetry modes) were refined to obtain the structure of the three compounds. Those "amplimodes" with lengths shorter than the isotropic thermal displacement will be nullified, in order to diminish the number of fitted parameters and increase the accuracy of the refinement. The starting amplitudes come from the analysis of the symmetry-adapted modes between the theoretical β-and β′ phases. The occupancy factor of the two possible sites (Wyckoff positions *4c*) for the RE in the *Pba2* space group, which came from one Wyckoff site *4e* in the $P\bar{4}2_1m$ space group were refined, in two different ways. First, assuming that one of the two sites is occupied exclusively by La or Er; thus, the occupancy factor of the second site for La and Er atom is refined, constraining these factors to sum 1. Second, the starting concentration of the synthesis was considered as valid, and the occupancy at each site was refined; thus, the occupancy factor for the La atom was constrained to sum 2-x, and for the Er atom to sum x. Finally, the thermal factors for each La, Er, and Mo atom type were refined and restricted to the same isotropic Debye-Waller factor.

2.3.2. Obtaining ε′(ω, T) and σ′(ω, T) curves and adjustments

The dielectric properties, i.e., the real part of the complex permittivity ε′ and the conductivity σ′, were studied for the three samples by measuring the complex impedance as a function of frequency for different temperatures Z*(ω). The complex permittivity ε*(ω) was calculated from the obtained value of Z*(ω) according to the following relation:

$$\varepsilon^*(\omega) = \frac{t}{i\omega\varepsilon_0 Z^*(\omega) A_c} \quad (1)$$

where ε_0 is the vacuum dielectric constant, A_c is the electrode area and t is the thickness of the sample. As well, the complex permittivity can be expressed as:

$$\varepsilon^*(\omega) = \varepsilon'(\omega) - i\frac{\sigma'(\omega)}{\omega} \quad (2)$$

where σ′(ω) is the real part of the complex conductivity.

The analysis of the conductivity spectra was performed based on the Universal Dielectric Response (UDR) model, an empirical power law that can describe the frequency and temperature dependence of the dielectric response in a wide range of disordered materials, including ionic glasses, non-stoichiometric crystals, polycrystalline and amorphous semiconductors [67–71]. Thus, the real part of the conductivity spectrum σ′(ω) tends towards the direct current conductivity (σ_{dc}) as the frequency decreases and shows a dispersive regime in which the conductivity increases strongly with frequency. Jonscher proposed the following dependence for the real part of conductivity [72]:

$$\sigma'(\omega) = \sigma_{dc} + A_\sigma \omega^s \quad (3)$$

where A_σ is a temperature-dependent constant and s is an exponent with a value between 0 and 1, which depends on the many-body interactions among the charge carriers. However, a slightly different version of the above equation was used in this work [73]:

$$\sigma'(\omega) = \sigma_{dc}\left[1 + cos\left(\frac{s\pi}{2}\right)\left(\frac{\omega}{\omega_p}\right)^s\right] \quad (4)$$

where ω_p is the frequency at which the change of slope in the real component of the complex conductivity occurs. By fitting the conductivity curves collected at different temperatures, the thermal dependence of the parameters (σ_{dc}, A_σ, ω_p *y s*) was obtained. With the study of the thermal dependence of these parameters, the permittivity and electrical conductivity, the transition temperatures can be detected. Moreover, the dynamics followed by the charges and dipoles that contribute to the anomalous behavior around the phase transition can be analyzed. To complete this study, the dielectric measures will be corroborated with the thermal dependence of the Er^{3+} emission.

3. Results and discussion

3.1. Ferroelectric phase at room temperature

3.1.1. Crystal structure

Fig. 1 shows the refinement results, and Table 1 presents the values of cell parameters, total "amplimodes" (calculated for the unit cell) and the agreement factors for the experimental and the theoretical results. The β′-$Gd_2(MoO_4)_3$ phase was identified in all diffractograms collected. The typical shift of the peaks towards the left (lower Bragg angles) was observed, related to the increase in volume by the concentration of La increasing. It is known that this solid solution expands for a broad

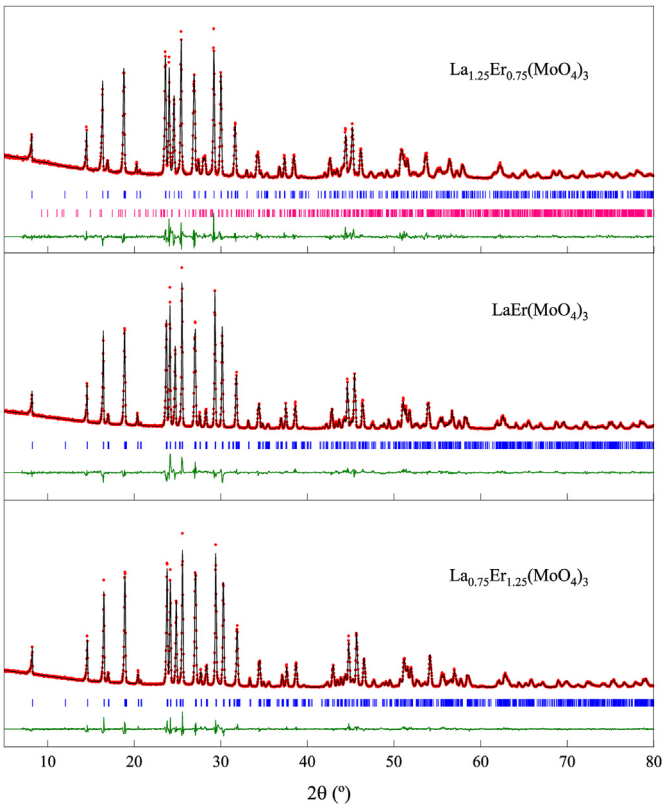

Fig. 1. Rietveld refinement results for the three compounds studied. Experimental observed data (red), calculated data (black) and the difference between the two (green) are indicated. In addition to the Bragg positions for each of the phases (blue) and the $La_2(MoO_4)_3$ phase (pink).

domain of x values; when the synthesis starts from oxides, x varies according to the quenching and annealing temperature and ranges from x = 0.4 to x = 1.15 [55]. This range has been extended until x = 1.25, carrying out the solid solution of the end compounds.

For the compound with the highest La concentration, the $La_2(MoO_4)_3$ phase was identified at low resolution and was also refined, leaving most parameters fixed (using published data [42]), thus improving the results of the total refinement. Regarding the intermediate compound LaEr(-$MoO_4)_3$, possible impurities of the final components could not be identified due to the background noise. The results obtained for the intermediate compound were very similar to those published by Hernández-Suárez et al. [56]. The best refinement results were obtained for the compound with the highest Er concentration.

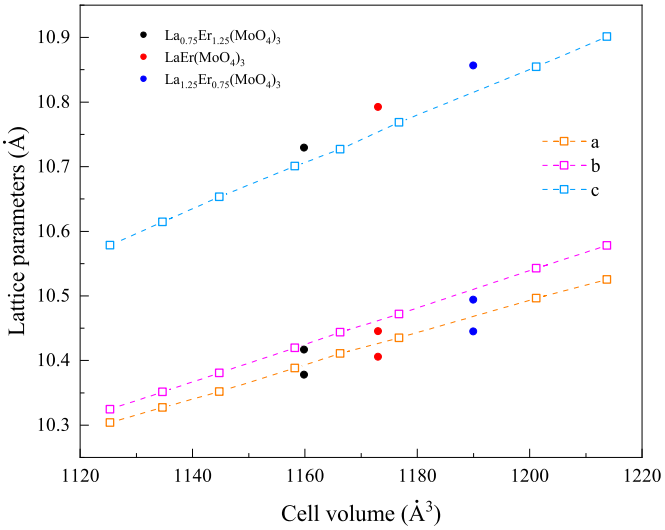

Fig. 2. Cell parameters for the three compounds $La_{2-x}Er_x(MoO_4)_3$ (x = 0.75 "•", 1 "•" and 1.25 "•") and for the lanthanide trimolybdate series β′-$RE_2(MoO_4)_3$ (with RE ≡ Pr, Nd, Sm, Eu, Gd, Tb, Dy and Ho) as a function of the cell volume.

In Fig. 2, the values of the calculated cell parameters *versus* the cell volume of our solid solutions can be seen in comparison with the complete RE trimolybdate family with the β′-phase. The *c* parameter is slightly longer and the *a* and *b* cell parameters are slightly shorter than those reported for the $RE_2(MoO_4)_3$ family. A smaller dispersion of the *a* and *b* parameters was observed as the Er concentration decreases, which is most evident in the pure trimolybdates when the lanthanide ionic radius decreases. This behavior is contrary to that typically observed

Table 1
Cell parameters, amplimodes and agreement factors obtained in the refinement of the diffractograms of $La_{2-x}Er_x(MoO_4)_3$ compounds with x = 0.75, 1 and 1.25. Upper values correspond to the first refinement and lower values to the second one.

	x = 0.75	x = 1	x = 1.25	x = 1 Theoretical β′ phase	x = 1 Theoretical β phase
***a* (Å)**	10.44582(17)	10.41296(11)	10.38488(10)	10.387276	7.4257
	10.44582(17)	10.41295(11)	10.38489(10)		
***b* (Å)**	10.49428(17)	10.45382(11)	10.42402(10)	10.614546	7.4257
	10.49429(17)	10.45380(11)	10.42404(10)		
***c*(Å)**	10.85791(15)	10.79972(10)	10.73736(9)	10.883800	10.8838
	10.85793(15)	10.79968(10)	10.73736(9)		
***V*(Å^3)**	1190.258(32)	1175.606(21)	1162.342(18)	1200	600
	1190.263(32)	1175.598(21)	1162.347(18)		
***Γ*$_1$ (Å)**	0.45(5)	1.00(4)	0.61(3)	0.0049	0
	0.45(5)	0.99(4)	0.64(3)		
***Γ*$_3$ (Å)**	0.53(11)	0.67(10)	0.68(8)	0.7110	0
	0.50(12)	0.73(9)	0.74(8)		
***M*$_2$+*M*$_4$ (Å)**	2.51(10)	2.35(7)	2.11(6)	1.8551	0
	2.48(10)	2.39(7)	2.11(6)		
***R*$_p$/*R*$_{wp}$ (%)**	9.40/10.4	11.9/12.6	12.2/13.2		
	9.57/10.4	12.1/12.7	12.2/13.2		
***R*$_{exp}$ (%)**	6.40	6.92	7.45		
	6.45	7.03	7.45		
***χ*2**	2.63	3.32	3.13		
	2.60	3.25	3.13		
***R*$_B$/*R*$_F$ (%)**	3.82/3.12	6.73/4.57	3.83/2.22		
	3.83/2.21	6.67/4.54	3.83/3.08		

when the cell volume decreases (e.g., by decreasing temperature or increasing pressure). In these cases, the *a* and *b* parameters are contracted anisotropically, and the *a*-*b* difference increases [39–41,56]. This longer distortion referred to the paraelectric phase, reflected in this cell parameters difference, was not observed in the compound with the higher concentration of Er, which "a priori" seems to feature an improved ferroelectric character. In addition, the *c* parameter experiences a contraction before the phase transition [39,41], and it necessary to know the atomic displacements in this direction depending on the x concentration.

From Table 1, the symmetry mode Γ_1 (compatible with the symmetry of the paraelectric phase) of the compound with x = 0.75 is the smallest, contributing to a minor global distortion because the cell volume of this compound is the closest to that of the prototype paraelectric phase (theoretical β-phase), which was calculated as explained in section 2.3 (structural characterization). On the other hand, the non-polar mode M_2+M_4 increases. This fact may be related to the difference between the *a* and *b* parameters. Their lengths increase as x decreases. It is worth noting that, as the Er concentration increases, the amplitude of the polar mode Γ_3 slightly increases; this may be indicative that the $La_{0.75}Er_{1.25}(MoO_4)_3$ compound enhances its ferroelectric properties.

Similar crystal structural parameters were obtained when the occupation factors were refined by using the two procedures and explained in section 2.3 (see Table 2 and Tables A1-A7). If these restrictions are not made, the refinement is less reliable, the standard deviation of the occupancy increases and it can converge to a false local minimum. The non-equivalent crystallographic sites for the La and Er were slightly differentiated with the second procedure, where the sum of the occupation factor for each type of lanthanide was constrained to the given x concentration; while they were clearly differentiated with the first one. Site 1 was preferably occupied by La and site 2 - by Er, in all compounds. The obtained x values were similar to those formulated for the synthesis. In the case of the Er-rich compound, the x concentration calculated with the first procedure was slightly higher than expected.

There were no significant changes in the atomic coordinates and amplitudes of the symmetry modes related to the heavier atoms. The structural differences, compared with the paraelectric phase, were related to the displacements of the oxygens (longer amplitudes), as expected. They are compared to those of the prototype compound, the theoretically calculated $LaEr(MoO_4)_3$ paraelectric structure, as explained in section 2.3. The compound $La_{0.75}Er_{1.25}(MoO_4)_3$ has longer shifts along the *c*-axis, according to the longer value of the amplitude of the mode Γ_3. It is not easy to calculate the spontaneous polarization from point charges because it is difficult to obtain the positions of the oxygens and their effective charges at these positions. However, the spontaneous polarizations $P_s(\Gamma_3)$ can be estimated from the sum of the displacements $\Delta(\Gamma_3)$, with the symmetry Γ_3, the electron charge and the cell volume V_{cell}:

$$P_s(\Gamma_3) = e \cdot \Delta(\Gamma_3)/V_{cell} \quad (5)$$

Results of P_s, between 0.7 and 0.9 μC/cm^2, are within the order of magnitude expected. Therefore, it is possible to confirm that the behavior of our compound is unexpectedly opposite to that of pure molybdates, where the ferroelectric properties increase with increasing the lanthanide ionic radius [19,20], although the behavior of the cell parameters is very similar.

To find the mechanisms responsible for this unexpected behavior, the lanthanide environments of the three compounds were compared. Table 3 shows the bond distances in the polyhedral coordination of both lanthanides for the compounds studied, including the theoretical structures. Sites with higher occupation of La atoms (La/Er) are distinguished from sites with higher occupation of Er atoms (Er/La). It was observed that the results of the intermediate compound had larger standard deviation and more dispersed lengths because the diffraction patterns had the worst resolution. In Fig. 3, the coordination environments of the two crystallographic sites were drawn. Thicker bonds indicate shortest distances. Longer RE … O distances do not belong to the coordination polyhedron are plotted with dashed lines. The symbols Mo(1) and Mo(12) belong to the same molybdenum atoms in the paraelectric, which forms the less symmetrical tetrahedron. The symbol Mo(2) belongs to the Mo atom which forms the most symmetrical tetrahedron in the paraelectric structure. The tetrahedra are quite regular, and the possible bond dispersions do not follow a clear pattern depending on the lanthanide concentration. The lanthanide polyhedra maintain the coordination number CN = 7 and the "capsulated" triangular prism geometry, forming polyhedral dimers, and reinforcing the shortest Ln … Ln distances (between 3.95 and 4.0 Å). Mainly, a shortening (lengthening) of the bond distances is observed at the sites with more Er (La) concentration, related to the prototype phase in which both sites are symmetrically equivalent. Fig. 3 and Table 3 show the closest distances corresponding to the second coordination sphere, with similar lengths to the shortest contacts: Ln … Ln, Mo···Mo and Mo … Ln. A shortening of the La···O(33) distance and a lengthening of the La···O(2) distance were observed. This behaviour can be explained within the "distortion theorem" of the Bond Valence Model [74] by the tendency of the La atom to have a coordination number 8. The bond shortening increases the sum of bond valences. Thus, the valence of La increased its value close to 3 v.u. (valence units), with an environment of 8 nearest oxygens atoms. In the case of the sites with more Er atoms, the two equivalent distances Er···O(3) and Er···O(32) are more similar, as in the prototype phase (paraelectric phase). However, an abnormal lengthening of one of the Er···O(22) coordination bonds occurs. In this case, the most common Er coordination number is 6. With this lengthening and the shortening of the remaining bonds, the sum of the bond valences of the Er atom approaches 3 v.u., with 6 nearest oxygen atoms.

This rearrangement makes possible a significant differentiation between the two sites, in contrast to the ferroelectric phase of other pure RE trimolybdates, with the crystallographic site environments of the lanthanides less distinguishable. Note that considering the theoretical β and β′ phases, in the first case there is one site for the La and Er atoms. In the second case, the first site is occupied only by La atoms and the second one only by Er atoms. When both atoms are exchanged the result is very similar, both sites can also be distinguished [56]. However, in $(Gd_{0.9}Yb_{0.1})_2(MoO_4)_3$, both sites for Yb are also heptacoordinated with oxygens atoms, but, in one site, the interatomic distances range from 2.24 to 2.48 Å, and in the other site, these distances range from 2.19 to 2.41 Å [52].

By representing the complete crystal structure for the three compounds, it can be observed how the coordination environments are affected by the displacements of the oxygen atoms. Fig. 4 shows a nearly *b*-axis view of these structures, with the polar axis (*c*-axis) along the vertical direction. The three types of molybdate tetrahedra are placed, without sharing vertices, in three different layers, perpendiculars to the *c*-axis. Between these layers, the lanthanides form coordination polyhedra

Table 2
Occupation factors of the La and Er atoms in the two different sites of the β′-$Gd_2(MoO_4)_3$ structure for two refinements with different constraints.

$La_{1.25}Er_{0.75}(MoO_4)_3$					
Occupation factors	Site 1 (La)	Site 1 (Er)	Site 2 (La)	Site 2 (Er)	x
2nd procedure	0.76 (11)	0.24(11)	0.49(11)	0.51(11)	0.75
1er procedure	1.0	0.0	0.22(9)	0.78(9)	0.78(9)
$LaEr(MoO_4)_3$					
Occupation factors	Site 1 (La)	Site 1 (Er)	Site 2 (La)	Site 2 (Er)	x
2nd procedure	0.503(3)	0.497(3)	0.503(3)	0.497(3)	1.0
1er procedure	1.03(7)	0.0	0.0	0.97(7)	0.97(7)
$La_{0.75}Er_{1.25}(MoO_4)_3$					
Occupation factors	Site 1 (La)	Site 1 (Er)	Site 2 (La)	Site 2 (Er)	x
2nd procedure	0.45(8)	0.55(8)	0.30(8)	0.70(8)	1.25
1er procedure	0.42(7)	0.58(7)	0.0	1.0	1.58(7)

Table 3
Bond distances in Å, involved in the coordination polyhedra for the compounds $La_{2-x}Er_x(MoO_4)_3$ and for the theoretical phases β and β' obtained from Ref. [56].

			x = 0.75	x = 1	x = 1.25	Theoretical β phase (Å)	Theoretical β′ phase (Å)
Mo(1)	−O(34)	1/2-x, −1/2 + y, z	1.71(3)	1.81(3)	1.69(3)	1.7426	1.7709
	−O(1)	x, y, z	1.76(8)	1.811(12)	1.69(5)	1.7612	1.7705
	−O(2)	1/2-x, −1/2 + y, z	1.87(3)	1.646(14)	1.765(9)	1.8067	1.8068
	−O(33)	x, −1+y, z	1.73(3)	1.77(3)	1.82(4)	1.7423	1.7767
Mo(12)	−O(12)	x, y, z	1.774(5)	1.811(12)	1.71(7)	1.7613	1.7686
	−O(3)	1/2 + x, 3/2-y, z	1.72(3)	1.657(21)	1.72(2)	1.7425	1.7725
	−O(22)	1/2 + x, 3/2-y, z	1.89(3)	1.748(18)	1.856(16)	1.8070	1.8290
	−O(32)	x, y, z	1.74(3)	2.100(21)	1.92(3)	1.7422	1.7733
Mo(2)	−O(43)	x, y, z	1.82(3)	1.79(5)	1.76(5)	1.776	1.7747
	−O(42)	x, y, −1+z	1.74(3)	1.77(4)	1.78(5)	1.769	1.7789
	−O(4)	x, y, −1+z	1.79(3)	2.04(4)	1.78(5)	1.7768	1.7812
	−O(44)	x, y, z	1.81(3)	1.92(5)	1.88(4)	1.7770	1.7754
La/Er	−O(43)	-x, 1-y, z	2.38(4)	2.39(4)	2.28(4)	2.2862	2.3687
(Site 1)	−O(44)	1/2-x, −1/2 + y, z	2.21(4)	2.34(4)	2.37(4)	2.2864	2.3708
	−O(34)	1/2-x, −1/2 + y, z	2.37(3)	2.28(3)	2.39(3)	2.3404	2.4329
	−O(12)	1/2-x, −1/2 + y, z	2.325(3)	2.280(12)	2.423(4)	2.3506	2.4441
	−O(2)	x, y, z	2.41(4)	2.459(13)	2.435(15)	2.4622	2.5139
	−O(33)	-x, 1-y, z	2.45(4)	2.40(3)	2.45(3)	2.3402	2.4555
	−O(2)	-x, 1-y, z	2.44(4)	2.633(14)	2.550(15)	2.4620	2.5469
	−O(33)	1/2-x, −1/2 + y, z	3.41(4)	3.50(3)	3.46(4)	3.8879	3.3414
	−O(34)	-x, 1-y, z	4.38(4)	4.23(3)	4.21(4)	3.8875	4.3564
Er/La	−O(4)	1/2 + x, 1/2-y, z	2.17(2)	1.92(4)	2.22(5)	2.2860	2.1968
(Site 2)	−O(22)	1 + x, −1+y, z	2.24(4)	2.26(3)	2.41(6)	2.4620	2.3700
	−O(1)	1-x, -y, z	2.322(3)	2.272(12)	2.415(3)	2.3507	2.2633
	−O(32)	1-x, 1-y, z	2.45(3)	2.321(21)	2.37(3)	2.3404	2.2981
	−O(42)	1-x, 1-y, z	2.38(2)	2.445(39)	2.40(5)	2.2863	2.2196
	−O(3)	1/2 + x, 1/2-y, z	2.44(3)	2.4541(21)	2.55(3)	2.3402	2.3502
	−O(22)	1-x, 1-y, z	2.54(4)	2.738(36)	2.45(6)	2.4622	2.4342
	−O(3)	1-x, 1-y, z	3.61(3)	3.873(20)	3.58(4)	3.8879	3.8530
	−O(32)	1/2 + x, 1/2-y, z	3.90(3)	3.895(21)	4.2(4)	3.8875	4.0432

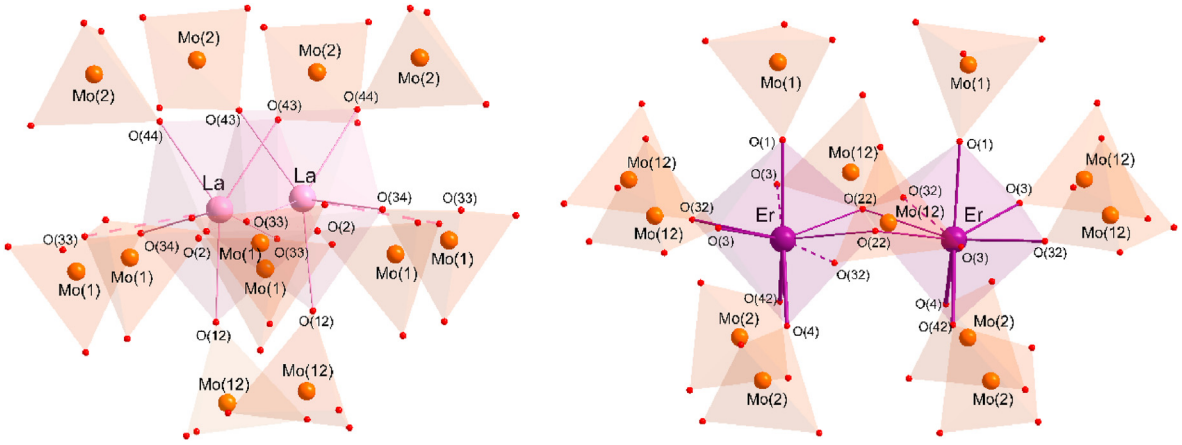

Fig. 3. Coordination environments of two sites in $La_{2-x}Er_x(MoO_4)_3$: site 1 with higher La concentration, at left and site 2 with higher Er concentration at right. The shortest bonds are thicker solid lines and those that do not belong to the coordination polyhedron are dashed lines.

by sharing the vertices of the tetrahedral anions $[MoO_4]^{2-}$. The black arrows indicate the oxygen shifts from the more symmetric prototype structure (paraelectric phase) with Γ_3 polar symmetry. It should be noted that the amplitudes (moduli of the vectors) have been plotted larger for better visualization. It can be seen that these displacements are longer in the compound with higher concentration of Er. The most pronounced shifts along the *c*-axis are observed for the oxygens, lengthening the Mo(1)–O(2) and Mo(12)–O(22) bonds, where O(2) and O(22) are equatorial oxygens in the lanthanide polyhedron. The displacements of the oxygens forming the four Mo(2)−O bonds, involving the oxygens: O(4), O(42), O(43), and O(44) are shorter and similar. They also form the shortest bonds of the LaO_7 and ErO_7 polyhedra. When the Er atom is introduced, the corresponding oxygen displacements diminish the component along the *c*-axis. These small displacements exhibit opposite direction to the displacements of the "equatorial" oxygens, that lengthen as the La concentration increases and shorten the amplitude of the Γ_3 mode; thus, the ferroelectric character is neglected in La-rich compounds. This behavior can be compared to that of the solid solution $Gd_xBi_{2-x}(MoO_4)_3$, where the ferroelectric properties also decrease (the Curie temperature decreases) when the Bi atom, with larger ionic radius than Gd, is substituted. The authors explain that this is due to the higher covalence in the coordination bonds of Bi, but they do not give structural details in their work [50]. In the case of the $Gd_xYb_{1-x}(MoO_4)_3$ solid solutions, anomalies appeared when Gd is substituted by Yb were also found, compared to other RE with longer ionic radii; but no current explanation is presented [51].

3.1.2. Ferroelectric hysteresis

Fig. 5 shows the ferroelectric hysteresis cycles (P-E) of the three samples obtained at room temperature and at 33 Hz, at different electric

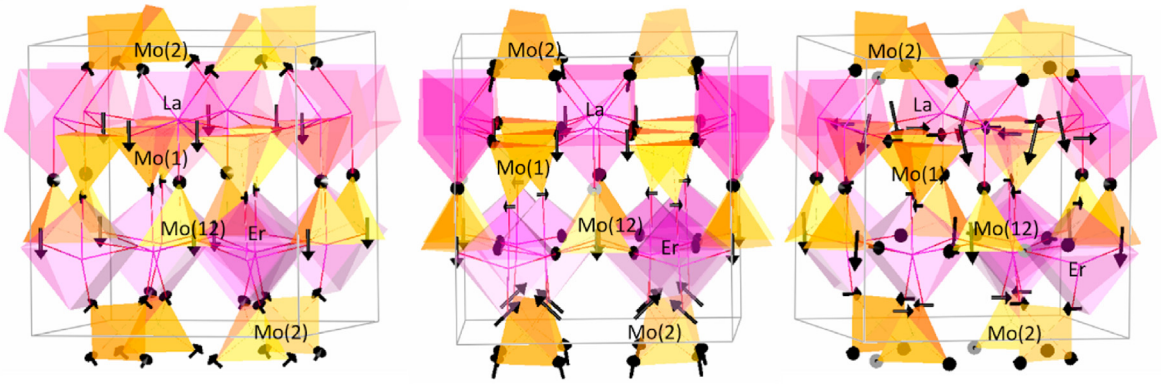

Fig. 4. Viewed almost perpendicular to the *b*-axis (the c-axis is taken as the vertical direction of the figure) of the β′-phase of: $La_{1.25}Er_{0.75}(MoO_4)_3$ (left), $LaEr(MoO_4)_3$ (center) and $La_{0.75}Er_{1.25}(MoO_4)_3$ (right). The black arrows indicate the displacements of the oxygens with Γ_3 mode symmetry with reference to the prototype β-phase.

fields between 5.88 and 33.3 kV/cm.

As can be seen, the size of the hysteresis cycles diminishes with increasing the lanthanum concentration under the same experimental conditions, which could be related to the loss of ferroelectric character (see also Fig. A3 of the supplementary material). The values of the remanent polarization (P_r) and maximun polarization (P_{max}) for $La_{0.75}Er_{1.25}(MoO_4)_3$ are higher than for $LaEr(MoO_4)_3$, which are almost one order of magnitude larger than for $La_{1.25}Er_{0.75}(MoO_4)_3$. The polarizations obtained from the larger cycles are of the same order of magnitude and with the same shape as the cycles recorded with the same applied field for β′-$Tb_2(MoO_4)_3$ single crystal, at room temperature [75]. The shape of the unsaturated cycle (at room temperature), which is normally associated with leakage current losses in proper ferroelectrics [76], could have another origin in the improper ones, since the primary structural order parameter (other than spontaneous polarization, which, is the secondary) controls the switching dynamics [77]. Moreover, the same synthesis conditions, similar width of the X-ray diffraction peaks and very similar values of the electrical conductivity measured with impedance spectroscopy, as will be discussed in section 3.2.2, support that we do not consider important differences in the microstructure of these samples depending on the lanthanide concentration. Then, the leakage currents losses, that may be present and will slightly affect the existing hysteresis loop, do not explain the order of magnitude variation in the cycle size. Certainly, these results are qualitatively in agreement with the structural results where the ferroelectric distortion is longer in the compounds with lower lanthanum concentrations. However, it is noteworthy that, contrary to what happens in the family of the improper ferroelectrics with formula $RE_2(MoO_4)_3$ [19,20], the spontaneous polarization increases, in a striking way, when the ionic radius of the lanthanide decreases for the solid solution studied. In the next sections, we will corroborate this unexpected enhancement of ferroelectric properties by increasing the Er concentration.

Finally, in order to confirm the origin of the hysteresis cycles, we have performed a preliminary test by increasing the temperature, without reaching the paraelectric phase due to equipment limitations. In Fig. A4 of the supplementary material, we show the decrease of the cycle size for $La_{0.75}Er_{1.25}(MoO_4)_3$, although P_{max} slightly increases, in the measured temperature range. This result is in agreement with the anomalous thermal dependence of the ferroelectric properties in the improper ferroelectrics. For the other two compounds, irregularities occur which are also difficult to interpret. Further analysis by reaching the Curie temperature and by comparing with thermodiffraction measurements is necessary to correlate with the thermal dependence of the crystal structure. Nevertheless, in the following sections, we have been able to verify this unusual thermal dependence of the electrical permittivity and conductivity, as well as the difficult detection of the Curie temperature.

3.2. Ferroelectric-paraelectric phase transition

3.2.1. Thermal Analysis

Fig. 6 shows the TG curves for the three compounds in a heating-cooling cycle. A slight mass loss, less than 2%, was calculated in the temperature range between 300 and 500 K during the heating stage, and it was not detected mass loss afterward. Thus, the three compounds are thermally stable up to 1173 K. The mass loss is due to the evaporation of moisture absorbed by the $Er_2(MoO_4)_3$ (hydrated). DSC results are not presented because the transition temperatures were not detected. These temperatures were analyzed with better results by dielectric and emission spectroscopy of Er^{3+}.

3.2.2. Dielectric properties

The thermal dependence of the real part of the complex dielectric permittivity ε_r' at different frequencies (50 and 100 kHz) for the three samples is shown in Fig. 7, observing anomalies in the temperature range

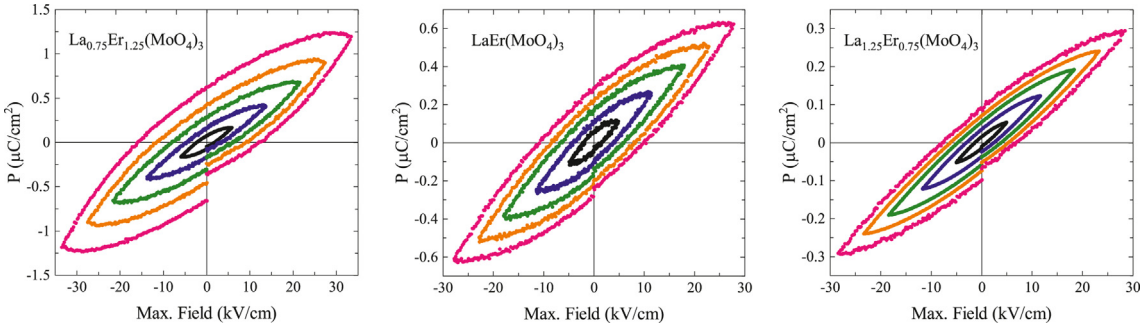

Fig. 5. Hysteresis cycles at room temperature and at 33 Hz for the series $La_{2-x}Er_x(MoO_4)_3$. The maximum applied fields for the three compounds are: 5.88 kV/cm (black), 13.72 kV/cm (blue), 21.57 kV/cm (green), 27.45 kV/cm (orange) and 33.33 kV/cm (pink).

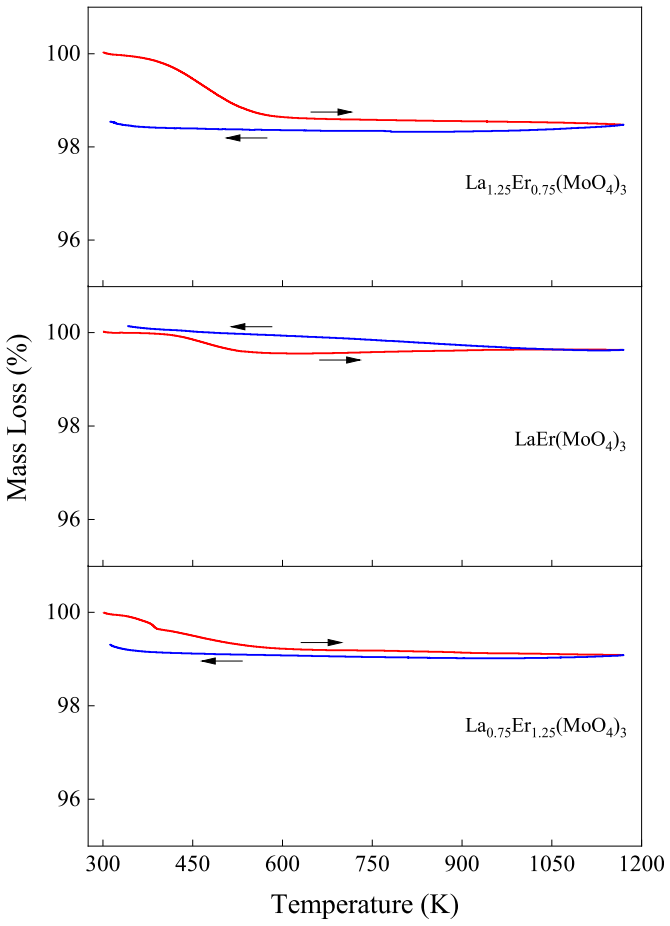

Fig. 6. TG curves for a heating (red) - cooling (blue) cycle for $La_{2-x}Er_x(MoO_4)_3$ samples.

between 608 and 613 K for $La_{0.75}Er_{1.25}(MoO_4)_3$ and between 348 and 353 K for $LaEr(MoO_4)_3$. Anomalies in the ε_r' curve were not detected between 300 and 800 K for $La_{1.25}Er_{0.75}(MoO_4)_3$. Moreover, it was observed that the transition temperature decreases with increasing La^{3+} concentration, and that ε_r' decreases slightly at this temperature. In general, this is typical for improper ferroelectrics; the ε_r' values vary very little in the vicinity of the transition temperatures [34]: between 66 and 62 for $La_{0.75}Er_{1.25}(MoO_4)_3$ and between 21 and 24 for $LaEr(MoO_4)_3$. These results disagree with those obtained by Elouadi et al. [55], who studied the same system, finding that the Curie temperature increased with lanthanum concentration. However, our results are consistent with the polarization values obtained in the hysteresis cycles and the larger distortion from the paraelectric phase. The Curie temperatures increase as the spontaneous polarization increases [22]. In the case of the intermediate composition, other authors obtain higher Curie temperatures: around 500 K [55] and 473 K [56]. These differences suggest that the La (or Er) concentration must be correctly determined. In our case, the shift of the diffractions peaks, the calculated cell parameters and the occupation factors reveal that concentrations are similar to the those formulated for the synthesis.

This dispersion of the real part of the complex dielectric permittivity leads to changes in the electrical conductivity. In Fig. 8, the results of the spectra for the real part of the complex electrical conductivity σ' as a function of frequency are presented, at different temperatures, for the sample $La_{0.75}Er_{1.25}(MoO_4)_3$, with the corresponding fits to Eq. (4). The curves of the other two samples, $LaEr(MoO_4)_3$ and $La_{1.25}Er_{0.75}(MoO_4)_3$, can be seen in Figs. A1 and A2 in the supplementary material. In the three Figures, at a fixed frequency, the conductivity increases very weakly with temperature. When temperature increases decompression is favored in not fully densified pellets and the conductivity is affected.

From the fit of the above three spectra to Eq. (4), the dependence of the *s* parameter on temperature is obtained (Fig. 9). This parameter is very sensitive to changes in the environment of the ions (phase transitions, distortions of the crystal structure, decompositions, etc.) which can affect the mobility of the charge carriers [78]. For $La_{0.75}Er_{1.25}(MoO_4)_3$, the *s* parameter reaches a minimum at 593 K ($s = 0.96$). This temperature almost coincides with the anomaly of ε_r' observed for the same compound. For $LaEr(MoO_4)_3$, this anomaly was not well detected and value of *s* is constant ($s = 0.99$) until 753 K. Then, *s* decreases with increasing temperature until 0.82 at 893 K. In comparison, for $La_{1.25}Er_{0.75}(MoO_4)_3$, *s* decreases from 0.99 at 653 K to 0.71 at 893 K. This abrupt decrease can be related to a new transition at higher temperature. The $RE_2(MoO_4)_3$ family of compounds undergoes the $\beta - \alpha$ transition, being α the high-temperature modulated scheelite phase [79]. The differences in the thermal dependence of carriers with the crystal structure depend on x concentration.

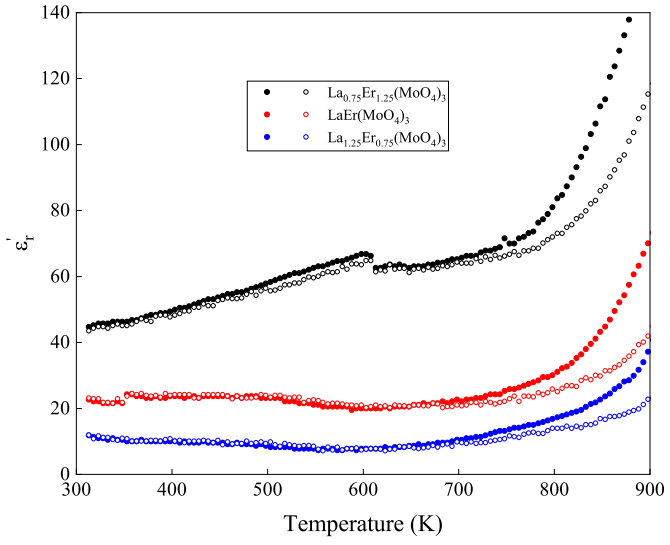

Fig. 7. Real part of the complex dielectric permittivity as a function of temperature at 50 kHz (filled circles) and 100 kHz (empty circles) for $La_{2-x}Er_x(MoO_4)_3$ samples.

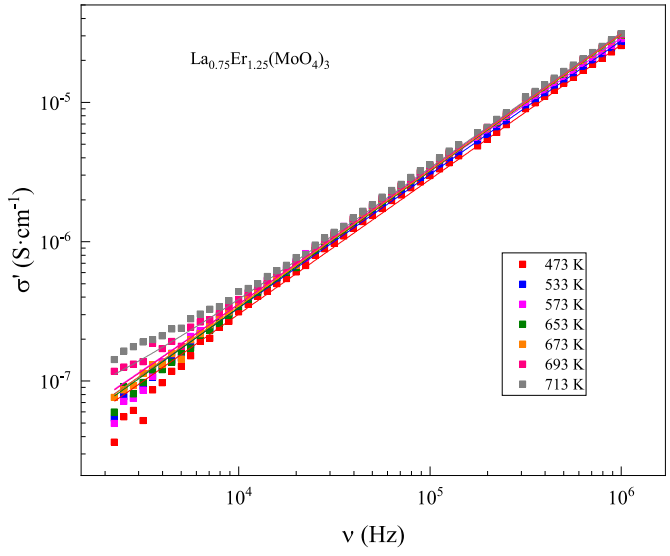

Fig. 8. Real part of the complex electrical conductivity as a function of frequency at various temperatures for $La_{0.75}Er_{1.25}(MoO_4)_3$ samples. The solid lines correspond to the fits to Eq. (4).

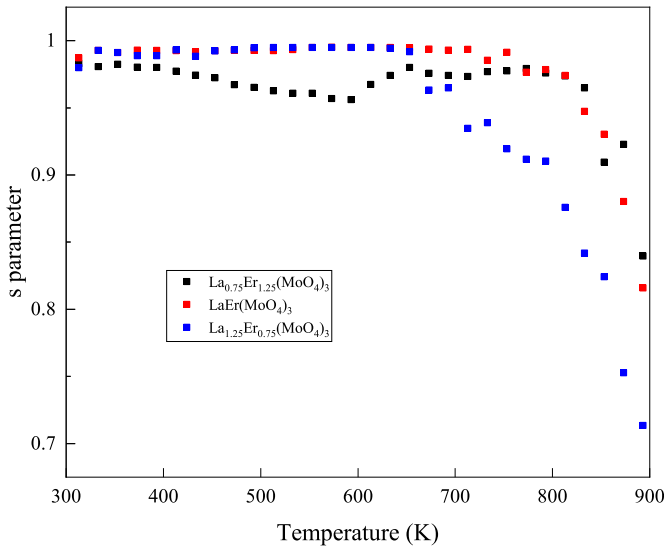

Fig. 9. Parameter s as a function of temperature for the three $La_{2-x}Er_x(MoO_4)_3$ samples.

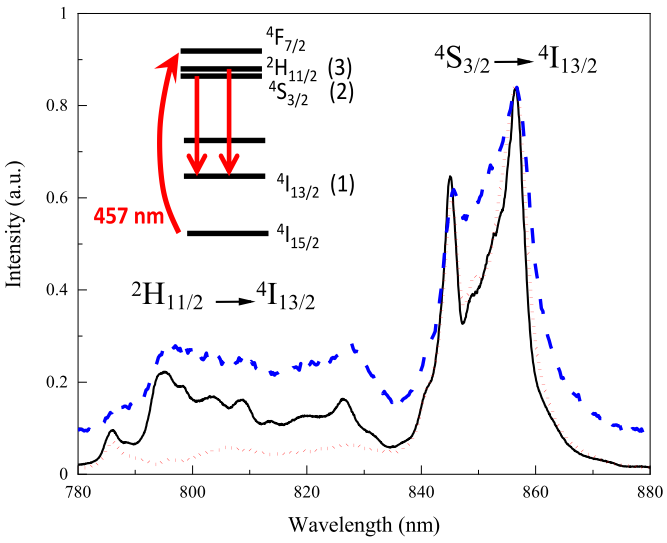

Fig. 10. Emission spectra obtained for the $La_{0.75}Er_{1.25}(MoO_4)_3$ (continuous line), $LaEr(MoO_4)_3$ (dotted line) and $La_{1.25}Er_{0.75}(MoO_4)_3$ (dashed line) samples at 410 K under the excitation at 457 nm. The inset shows the simplified scheme level of the Er^{3+} ions and the transitions involved in the excitation and emissions bands.

3.2.3. *Emission spectra of Er^{3+}*

Emission spectroscopy was included to corroborate the transition temperatures observed in the dielectric characterization. It is a common characterization technique for ferroelectrics since lanthanide ions are very sensitive to structural changes [80]. Therefore, these ions can be used as optical probes to detect structural phase transitions.

The emission spectra of the $La_{0.75}Er_{1.25}(MoO_4)_3$, $LaEr(MoO_4)_3$, and $La_{1.25}Er_{0.75}(MoO_4)_3$ samples obtained at 410 K under an excitation at 457 nm are shown in Fig. 10. These spectra show the typical emission bands coming from Er^{3+} ions corresponding to the $^2H_{11/2} \rightarrow {}^4I_{13/2}$ (800–830 nm) and $^4S_{3/2} \rightarrow {}^4I_{13/2}$ (840–860 nm) transitions. Moreover, as can be seen in the spectra, these bands show sharp peaks due to the Stark splitting of the involved levels, indicating that the Er^{3+} ions are well incorporated in the crystal structure.

Emitting $^2H_{11/2}$ and $^4S_{3/2}$ levels are used as temperature sensors due to the thermal dependence of the ratio of their emissions. Moreover, these levels are thermally coupled, and the intensity ratio (R) of the $^2H_{11/2} \rightarrow {}^4I_{13/2}$ (800–830 nm) and $^4S_{3/2} \rightarrow {}^4I_{13/2}$ (840–860 nm) transitions follows a Boltzmann distribution [7,81,82]. According to the simplified scheme level shown in the inset of Fig. 10, the $^2H_{11/2}$, $^4S_{3/2}$, and $^4I_{13/2}$ levels are designated by 3, 2 and 1, respectively, so the intensity ratio can be expressed as:

$$R = \frac{A_3\beta_3 g_3 h\nu_3}{A_2\beta_2 g_2 h\nu_2} exp\left(\frac{E_{32}}{K_B T}\right) = Aexp\left(\frac{E_{32}}{K_B T}\right) \quad (6)$$

where A_i is the spontaneous radiative rate of the i-th level, β_i represent the branching ratio of the transition, g_i is the degeneracy of each level and $h\nu_i$ is the average photon energy of each band. Finally, K_B is the Boltzmann constant and E_{32} is the average energy gap between the excited levels.

In Fig. 11(a), the intensity ratio of the $^2H_{11/2} \rightarrow {}^4I_{13/2}$ and $^4S_{3/2} \rightarrow {}^4I_{13/2}$ emissions is shown as a function of the temperature for the $La_{0.75}Er_{1.25}(MoO_4)_3$ sample. A good fitting is obtained to Eq. (6) with A = 34.0 and $E_{32} = 829\ cm^{-1}$, in the temperature range from 400 to 600 K. However, about 610 K, there is a slight change in the dependence (Fig. 11(b)). As can be seen in Fig. 11(b), the change in slope around 610 K obtained for the intensity ratio coincides with the anomaly observed for the real part of the complex dielectric permittivity (ε_r') around this temperature (Fig. 7).

Similarly, Fig. 12(a) shows the emission intensity ratios $^2H_{11/2} \rightarrow {}^4I_{13/2}$ (800–830 nm) and $^4S_{3/2} \rightarrow {}^4I_{13/2}$ (840–860 nm) as a function of temperature for the $LaEr(MoO_4)_3$ sample, from 300 to 520 K. The relationship shows a good fit to Eq. (6) with A = 2.5 and $E_{32} = 862\ cm^{-1}$. In this case, the small change occurs at 350 K, coinciding with the observed change for ε_r' in this sample (Fig. 7) (see Fig. 12(b)).

According to Figs. 11 and 12, the changes in the intensity ratio show a discontinuous thermal dependence at 610 and 350 K for the samples $La_{0.75}Er_{1.25}(MoO_4)_3$ and $LaEr(MoO_4)_3$, respectively. Furthermore, changes in ε_r' were also observed at these temperatures for both samples. These results confirm a phase transition for our two samples that affects the position of the Er^{3+} ions in the matrix and produces a shift in the emission bands. However, for the sample $La_{1.25}Er_{0.75}(MoO_4)_3$, discontinuous changes in the emission intensity ratio or the real part of the complex dielectric permittivity as a function of temperature were not detected, indicating that a phase transition was not observed for this sample in this temperature range. It is expected that the transition undergoes at lower temperatures, according to a lower spontaneous polarization (maximum and remanent). Therefore, confirming that the ferroelectric properties increase with Er^{3+} composition, contrary to the expectations. Moreover, a high variation of these properties is obtained as a function of the concentration x. For example, the transition temperature increases from 350 to 610 K, while the average ionic radius of the lanthanides in the solid solutions ranges from Gd^{3+} and Nd^{3+} radii and the transition temperatures of the respective trimolybdates increase from 430 to 500 K.

4. Conclusions

Three polycrystalline compounds with the formula $La_{2-x}Er_x(MoO_4)_3$ were synthesized with x = 0.75, 1, and 1.25 by the ceramic synthesis route. The range of concentrations was extended by taking $La_2(MoO_4)_3$ and $Er_2(MoO_4)_3$ (hydrated compound) as starting elements instead of lanthanide and molybdenum oxides. The X-ray diffraction patterns were identified and refined with the β'-$Gd_2(MoO_4)_3$ structure type, using the Rietveld method and refining the so-called "amplimodes" instead of the atomic coordinates. The cell parameters *a* and *b* were shortened, and the cell parameter *c* was lengthened compared with the cell parameters of the isostructural $RE_2(MoO_4)_3$ family. The lengthening in the *c* direction allows larger displacements of the oxygen atoms, increasing the amplitude of the polar symmetry mode Γ_3, which is responsible of the spontaneous polarization. The two lanthanide coordination environments were distinguished depending on the higher or lower Er or La occupation. The

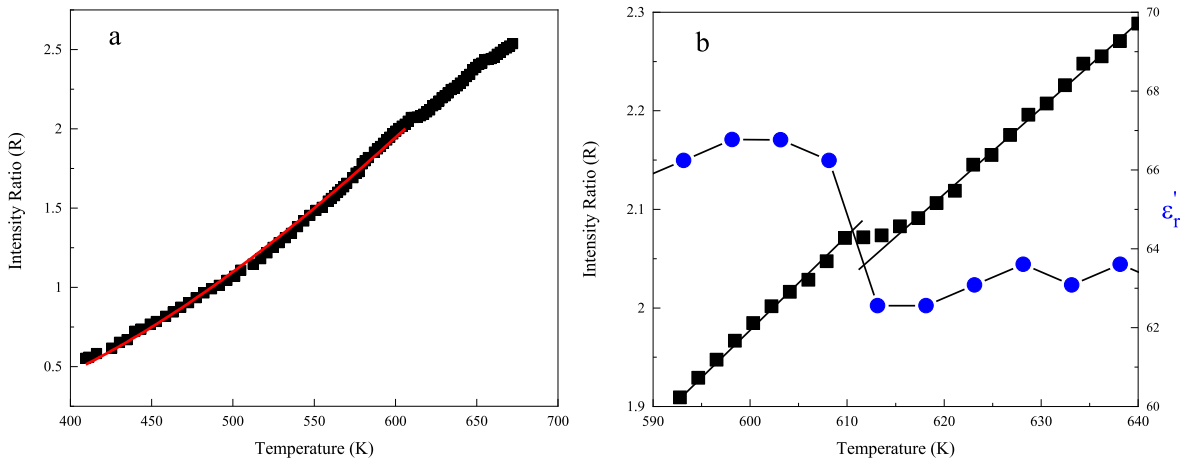

Fig. 11. (a) Dependence of the intensity ratio of the emission bands $^2H_{11/2} \rightarrow {}^4I_{13/2}$ (800–830 nm) and $^4S_{3/2} \rightarrow {}^4I_{13/2}$ (840–860 nm) with the temperature for the $La_{0.75}Er_{1.25}(MoO_4)_3$ sample. The red solid line is the fit to Eq. (6) with A = 34.0 and $E_{32} = 829\ cm^{-1}$. (b) Dependence of the intensity ratio of Fig. 11(a) in the range of 610 K (■) and dependence of the dielectric constant with the temperature (•).

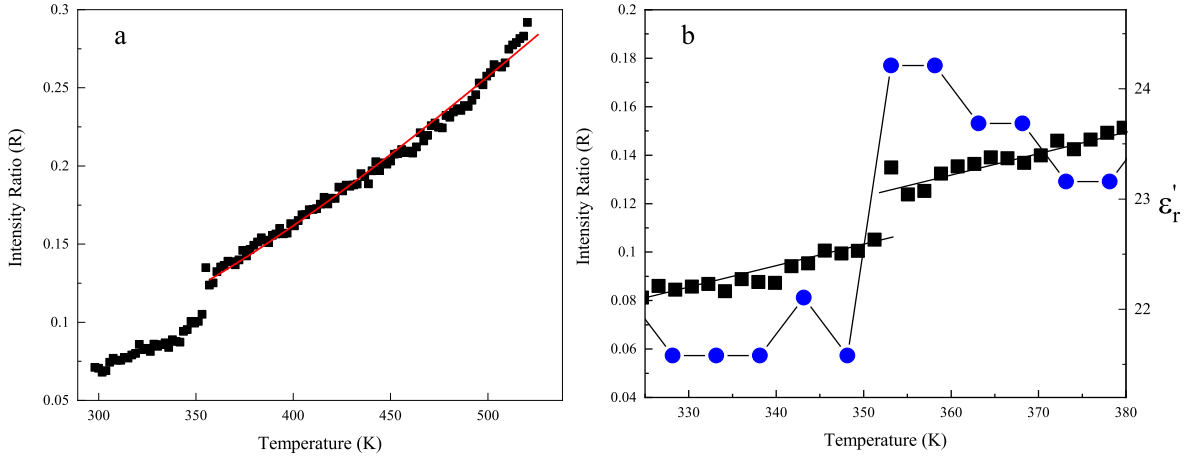

Fig. 12. (a) Dependence of the intensity ratio of the emission bands $^2H_{11/2} \rightarrow {}^4I_{13/2}$ (800–830 nm) and $^4S_{3/2} \rightarrow {}^4I_{13/2}$ (840–860 nm) with the temperature for the $LaEr(MoO_4)_3$ sample. The red solid line is the fit to Eq. (6) with A = 2.5 and $E_{32} = 862\ cm^{-1}$. b) Dependence of the intensity ratio of Fig. 12(a) in the range of 350 K (■) and dependence of the dielectric constant with the temperature (•).

oxygen atoms involved in the longest and asymmetric coordination bonds play an essential role in shaping both environments. However, the displacements associated with the oxygen atoms involved in the shortest distances, which belong to the more symmetric $[MoO_4]^{2-}$ tetrahedron, determine the increase in the distortion with polar symmetry, featuring a more ferroelectric behavior for more Er-rich compounds.

Comparing the ferroelectric hysteresis cycles of the three compounds, an increase of the maximum and remanent polarizations as the Er concentration increases was found. Therefore, the $La_{0.75}Er_{1.25}(MoO_4)_3$ compound exhibits enhanced ferroelectric properties, according to the crystal structure analysis and in contrast to the $RE_2(MoO_4)_3$ family, where the ferroelectric properties increase with increasing the lanthanide ionic radius. Moreover, the polarization increases by almost an order of magnitude for this compound; compared to other improper ferroelectrics.

Regarding the impedance spectroscopy measurements, the ferroelectric-paraelectric phase transition was observed from the electrical permittivity curves ε_r' for $La_{0.75}Er_{1.25}(MoO_4)_3$ around 610 K and for $LaEr(MoO_4)_3$ around 350 K. The phase transition was not detected for the La-rich compound in the temperature range studied. The results of the curve fitting of σ′ using the UDR model confirmed the Curie temperature of the more Er-rich compound and its enhanced ferroelectric behavior. Moreover, the intensity ratio of the $^2H_{11/2} \rightarrow {}^4I_{13/2}$ y $^4S_{3/2} \rightarrow {}^4I_{13/2}$ Er^{3+} emissions was used as an optical probe, detecting the same Curie temperature as with dielectric spectroscopy for the two Er-rich compounds.

In addition to the current interest of the optical properties (especially upconversion and fluorescence thermometry), most investigated in the intermediate compound (with x = 1), we want to highlight the unpredicted behavior of this series of solid solutions compared to the family of improper ferroelectrics $RE_2(MoO_4)_3$, where the change of La or Er concentration allows a wide tuning of the ferroelectric properties. This series of compounds experiences a broader range of transition temperatures, from room temperature to 600 K, where the electrical permittivity is practically constant, and the polarization varies by one order of magnitude ($P_{max} = 0.12–1.20\ \mu C/cm^2$). Undoubtedly, they belong to a relevant family of multiferroic and multifunctional crystalline matrices, which are also suitable for hosting the whole lanthanide series.

CRediT authorship contribution statement

G. Gil-de-Cos: Conceptualization, Methodology, Visualization, Investigation, Supervision, Writing – original draft, Writing – review & editing. **M.E. Torres:** Conceptualization, Methodology, Visualization, Investigation, Supervision, Writing – original draft, Writing – review & editing. **C. González-Silgo:** Conceptualization, Methodology, Visualization, Investigation, Supervision, Writing – original draft, Writing –

review & editing. **K. Soler-Carracedo:** Visualization, Investigation, Methodology, Writing – original draft. **I.R. Martín:** Visualization, Investigation, Writing – original draft. **F. Rivera-López:** Visualization, Investigation, Writing – original draft. **S. Rodríguez-Rodríguez:** Visualization, Investigation.

Declaration of competing interest

The authors declare that they have no known competing financial interests or personal relationships that could have appeared to influence the work reported in this paper.

Data availability

Data will be made available on request.

Acknowledgements

This work has been partially supported by the Agencia Canaria de Investigación, Innovación y Sociedad de la Información of Gobierno Autónomo de Canarias (PROID2021010027, PROID202101010 and PROID2020010067) and by the Ministerio de Ciencia e Innovación of Spain (MICIIN) under the National Program of Sciences and Technological Materials (PID2019-106383 GB-C44 and PID2019-107335RA-I00). We also wish to thank the Research Support Services of the University of La Laguna, especially the x-ray Diffraction (SIDIX) and Thermal Analysis (SAT-LCPM) facilities.

Appendix A. Supplementary data

Supplementary data to this article can be found online at https://doi.org/10.1016/j.jssc.2022.123462.

References

[1] B.M.J. Smets, Phosphors based on rare-earths, a new era in fluorescent lighting, Mater. Chem. Phys. 16 (1987) 283–299, https://doi.org/10.1016/0254-0584(87)90103-9.
[2] J.W.H. van Krevel, J.W.T. van Rutten, H. Mandal, H.T. Hintzen, R. Metselaar, Luminescence properties of terbium-,cerium-, or europium-doped α-sialon materials, J. Solid State Chem. 165 (1) (2002) 19–24, https://doi.org/10.1006/jssc.2001.9484.
[3] P. Pust, P.J. Schmidt, W. Schnick, A revolution in lighting, Nat. Mater. 14 (2015) 454–458, https://doi.org/10.1038/nmat4270.
[4] A.A. Kaminskii, Laser Crystals: Their Physics and Properties, Springer Berlin, Heidelberg, 2013, https://doi.org/10.1007/978-3-540-34838-2.
[5] T. Aitasalo, P. Dereń, J. Hölsä, H. Jungner, J.C. Krupa, M. Lastusaari, J. Legendziewicz, J. Niittykoski, W. Stręk, Persistent luminescence phenomena in materials doped with rare earth ions, J. Solid State Chem. 171 (1–2) (2003) 114–122, https://doi.org/10.1016/S0022-4596(02)00194-9.
[6] J. Shen, L.D. Sun, C.H. Yan, Luminescent rare earth nanomaterials for bioprobe applications, Dalton Trans. 42 (2008) 5687–5697, https://doi.org/10.1039/B805306E.
[7] K. Saidi, M. Dammark, Upconversion luminescence and optical temperature sensing characteristics of Er3+/Yb3+ codoped $Na_3Gd(PO_4)_2$ phosphors, J. Solid State Chem. 300 (2021), 122214, https://doi.org/10.1016/j.jssc.2021.122214.
[8] N. Zhang, D. Chen, F. Niu, S. Wang, L. Qin, Y. Huang, Enhanced visible light photocatalytic activity of Gd-doped $BiFeO_3$ nanoparticles and mechanism insight, Sci. Rep. 6 (2016) 1–11, https://doi.org/10.1038/srep26467.
[9] Yuhong Zhang, Huaxing Zhang, Yongxi Xu, Yanguang Wang, Significant effect of lanthanide doping on the texture and properties of nanocrystalline mesoporous TiO2, J. Solid State Chem. 177 (10) (2004) 3490–3498, https://doi.org/10.1016/j.jssc.2004.05.026.
[10] A.M. Kaczmarek, R. Van Deun, Rare earth tungstate and molybdate compounds–from 0D to 3D architectures, Chem. Soc. Rev. 42 (2013) 8835–8848, https://doi.org/10.1039/C3CS60166H.
[11] L. Xu, C. Lu, Z. Zhang, X. Yang, W. Hou, Various self-assembled three-dimensional hierarchical architectures of $La_2(MoO_4)_3$: controlled synthesis, growth mechanisms, luminescence properties and adsorption activities, Nanoscale 2 (2010) 995–1005, https://doi.org/10.1039/B9NR00392D.
[12] V.V. Atuchin, A.S. Aleksandrovsky, O.D. Chimitova, T.A. Gavrilova, A.S. Krylov, M.S. Molokeev, A.S. Oreshonkov, B.G. Bazarov, J.G. Bazarova, Synthesis and spectroscopic properties of monoclinic α-$Eu_2(MoO_4)_3$, J. Phys. Chem. C 118 (2014) 15404–15411. https://pubs.acs.org/doi/abs/10.1021/jp5040739.
[13] W. Xia, X. Wang, Z. Fu, S. Zhou, S. Zhang, J.H. Jeong, Tuning of crystal phase and luminescence properties of $Gd_2(MoO_4)_3$: Dy^{3+} phosphors, Mater. Res. Bull. 47 (2012) 2535–2540, https://doi.org/10.1016/j.materresbull.2012.05.003.
[14] G. Yi, B. Sun, F. Yang, D. Chen, Y. Zhou, J. Cheng, Synthesis and characterization of high-efficiency nanocrystal up-conversion phosphors: ytterbium and erbium codoped lanthanum molybdate, Chem. Mater. 14 (2002) 2910–2914, https://doi.org/10.1021/cm0115416.
[15] Y. Tian, B. Chen, B. Tian, R. Hua, J. Sun, L. Cheng, H. Zhong, X. Li, J. Zhang, Y. Zheng, T. Yu, L. Huang, Q. Meng, Concentration-dependent luminescence and energy transfer of flower-like $Y_2(MoO_4)_3$: Dy^{3+} phosphor, J. Alloys Compd. 509 (2011) 6096–6101, https://doi.org/10.1016/j.jallcom.2011.03.034.
[16] Y.R. Parauha, R.S. Yadav, S.J. Dhoble, Enhanced photoluminescence via doping of phosphate, sulphate and vanadate ions in Eu^{3+} doped $La_2(MoO_4)_3$ downconversion phosphors for white LEDs, 105974, Opt Laser. Technol. 124 (2020), https://doi.org/10.1016/j.optlastec.2019.105974.
[17] Rajesh Adhikari, Gobinda Gyawali, Hun Sung, Cho, R. Narro-García, Tohru Sekino, Wohn Soo, Lee, Er^{3+}/Yb^{3+} co-doped bismuth molybdate nanosheets upconversion photocatalyst with enhanced photocatalytic activity, J. Solid State Chem. 209 (2014) 74–81, https://doi.org/10.1016/j.jssc.2013.10.028.
[18] L.E. Cross, A. Fouskova, S.E. Cummins, Gadolinium molybdate, a new type of ferroelectric crystal, Phys. Rev. Lett. 21 (1968) 812, https://doi.org/10.1103/PhysRevLett.21.812.
[19] L.H. Brixner, P.E. Bierstedt, A.W. Sleight, M.C. Licis, Precision parameters of some $Ln_2(MoO_4)_3$-type rare earth molybdates, Mater. Res. Bull. 6 (1971) 545–554, https://doi.org/10.1016/0025-5408(71)90003-1.
[20] L.H. Brixner, J.R. Barkley, W. Jeitschko, Rare earth molybdates (VI), Handb. Phys. Chem. Rare Earths 3 (1979) 609–654, https://doi.org/10.1016/S0168-1273(79)03013-0.
[21] L.H. Brixner, A.W. Sleight, M.S. Licis, Cell dimensions of the molybdates $La_2(MoO_4)_3$, $Ce_2(MoO_4)_3$, $Pr_2(MoO_4)_3$, and $Nd_2(MoO_4)_3$, J. Solid State Chem. 5 (2) (1972) 247–249, https://doi.org/10.1016/0022-4596(72)90035-7.
[22] S.C. Abrahams, Structure relationship to dielectric, elastic and chiral properties, Acta Crystallogr., Sect. A: Found. Crystallogr. 50 (1994) 658–685, https://doi.org/10.1107/S010876739400573810.1107/S0108768199003730.
[23] A.A. Kaminski, Orthorhombic ferroelectric and ferroelastic $Gd_2(MoO_4)_3$ crystal – a new many-purposed nonlinear and optical material: efficient multiple stimulated Raman scattering and CW and tunable second harmonic generation, Opt. Mater. 7 (1997) 59–73, https://doi.org/10.1016/S0925-3467(97)00006-2.
[24] H. Hao, H. Lu, R. Meng, Z. Nie, G. Ao, Y. Song, Y. Wang, X. Zhang, Thermometry via Au island-enhanced luminescence of Er^{3+}/Yb^{3+} co-doped $Gd_2(MoO_4)_3$ thin films, J. Alloys Compd. 695 (2017) 2065–2071, https://doi.org/10.1016/j.jallcom.2016.11.045.
[25] Y. Tsukada, T. Honma, T. Komatsu, Self-powdering and nonlinear optical domain structures in ferroelastic β′-$Gd_2(MoO_4)_3$ crystals formed in glass, J. Solid Chem. 182 (8) (2009) 2269–2273, https://doi.org/10.1016/j.jssc.2009.06.009.
[26] E. Coy, P. Graczyk, L. Yate, K. Załęski, J. Gapiński, P. Kuświk, S. Mielcarek, F. Stobiecki, B. Mróz, C. Ferrater, S. Jurga, Second harmonic generation response in thermally reconstructed multiferroic β′-$Gd_2(MoO_4)_3$ thin films, Sci. Rep. 7 (2017) 1–9, https://doi.org/10.1038/s41598-017-12370-y.
[27] A.P. Levanyuk, D.G. Sannikov, Improper ferroelectrics, Sov. Phys. Usp. 17 (1974) 199, https://doi.org/10.1070/PU1974v017n02ABEH004336.
[28] A.W. Sleight, L.H. Brixner, A new ferroelastic transition in some $A_2(MO_4)_3$ molibdates and tungstates, J. Solid State Chem. 7 (2) (1973) 172–174, https://doi.org/10.1016/0022-4596(73)90152-7.
[29] W. Jeitschko, A comprehensive X-ray study of the ferroelectric–ferroelastic and paraelectric–paraelastic phases of $Gd_2(MoO_4)_3$, Acta Crystallogr. B28 (1972) 60–76, https://doi.org/10.1107/S0567740872001876.
[30] J.C. Toledano, Symmetry-determined phenomena at crystalline phase transitions, J. Solid State Chem. 27 (1) (1979) 41–49, https://doi.org/10.1016/0022-4596(79)90143-9.
[31] J.M. Perez-Mato, D. Orobengoa, M.I. Aroyo, Mode crystallography of distorted structures, Acta Cryst. A: Foundations Crystallogr. 66 (2010) 558–590, https://doi.org/10.1107/S0108767310016247.
[32] E.T. Keve, S.C. Abrahams, J.L. Bernstein, Ferroelectric ferroelastic paramagnetic β-$Gd_2(MoO_4)_3$ crystal structure of the transition-metal molybdates and tungstates, VI. J. Chem. Phys. 54 (1971) 3185–3194, https://doi.org/10.1063/1.1675308.
[33] K. Aizu, General consideration of ferroelectrics and ferroelastics such that the electric susceptibility or elastic compliance is temperature independent in the prototypic phase, J. Phys. Soc. Jpn. 33 (1972) 629–634, https://doi.org/10.1143/JPSJ.33.629.
[34] E. Bousquet, M. Dawber, N. Stucki, C. Lichtensteiger, P. Hermet, S. Gariglio, J.M. Triscone, P. Ghosez, Improper ferroelectricity in perovskite oxide artificial superlattices, Nature 452 (2008) 732–736, https://doi.org/10.1038/nature06817.
[35] J. Nordlander, M. Campanini, M.D. Rossell, R. Erni, Q.N. Meier, A. Cano, N.A. Spaldin, M. Fiebig, M. Trassin, The ultrathin limit of improper ferroelectricity, Nat. Commun. 10 (2019) 5591, https://doi.org/10.1038/s41467-019-13474-x.
[36] E. Sawaguchi, L.E. Cross, Spontaneous polarization of $Gd_2(MoO_4)_3$, J. Appl. Phys. 44 (1973) 2541–2544, https://doi.org/10.1063/1.1662610.
[37] T. Wakamatsu, K. Tanabe, I. Terasaki, H. Taniguchi, Improper ferroelectrics as high-efficiency energy conversion materials, Phys. Status Solidi 11 (2017), 1700009, https://doi.org/10.1002/pssr.201700009.
[38] V.S. Bondarev, E.A. Mikhaleva, M.V. Gorev, I.N. Flerov, Direct and indirect studies of the electrocaloric effect in single crystalline ferrielectric $(NH_4)_2SO_4$, J. Alloys Compd. 892 (2022), 162130, https://doi.org/10.1016/j.jallcom.2021.162130.

[39] C. Guzmán-Afonso, J. López-Solano, C. González-Silgo, S.F. León-Luis, E. Matesanz, A. Mujica, Pressure evolution of two polymorphs of $Tb_2(MoO_4)_3$, High Pres. Res. 34 (2014) 184–190, https://doi.org/10.1080/08957959.2014.895342.

[40] C. González-Silgo, C. Guzmán-Afonso, V.M. Sánchez-Fajardo, S. Acosta-Gutiérrez, A. Sánchez-Soares, M.E. Torres, N. Sabalisck, E. Matesanz, J. Rodríguez-Carvajal, Polymorphism in $Ho_2(MoO_4)_3$, Powder Diffr. 28 (2013) S33–S40, https://doi.org/10.1017/S0885715613001176.

[41] M. Keskar, N.D. Dahale, K. Krishnan, N.K. Kulkarni, Thermal expansion studies of $Gd_2Mo_3O_{12}$ and $Gd_2W_3O_{12}$, Mater. Res. Bull. 44 (2009) 901–905, https://doi.org/10.1016/j.materresbull.2008.08.014.

[42] W. Jeitschko, Crystal structure of $La_2(MoO_4)_3$ a new ordered defect scheelite type, Acta Crystallogr. B29 (1973) 2074–2081, https://doi.org/10.1107/S0567740873006138.

[43] J.S.O. Evans, T.A. Mary, A.W. Sleight, Negative thermal expansion in $Sc_2(WO_4)_3$, J. Solid State Chem. 137 (1998) 148–160, https://doi.org/10.1006/jssc.1998.7744.

[44] J.S.O. Evans, T.A. Mary, A.W. Sleight, Negative thermal expansion in a large molybdate and tungstate family, J. Solid State Chem. 133 (2) (1997) 580–583, https://doi.org/10.1006/jssc.1997.7605.

[45] V.A. Morozov, M.V. Raskina, B.I. Lazoryak, K.W. Meert, K. Korthout, P.F. Smet, D. Poelman, N. Gauquelin, J. Verbeeck, A.M. Abakumov, J. Hadermann, Crystal structure and luminescent properties of $R_{2-x}Eu_x(MoO_4)_3$ (R= Gd, Sm) red phosphors, Chem. Mater. 26 (2014) 7124–7136, https://doi.org/10.1021/cm503720s.

[46] M.V. Raskina, V.A. Morozov, A.V. Pavlenko, I.G. Samatov, I.V. Arkhangel'skii, S.Y. Stefanovich, B.I. Lazoryak, Structure and luminescent properties of solid solutions $Sm_{2-x}Eu_x(MoO_4)_3$, Russ. J. Inorg. Chem. 60 (2015) 84–91, https://doi.org/10.1134/S0036023615010118.

[47] S.F. Wang, K. Koteswara Rao, Y.R. Wang, Y.F. Hsu, S.H. Chen, Y.C. Lu, Structural characterization and luminescent properties of a red phosphor series: $Y_{2-x}Eu_x(MoO_4)_3$ (x= 0.4 – 2.0), J. Am. Ceram. Soc. 92 (2009) 1732–1738, https://doi.org/10.1111/j.1551-2916.2009.03118.x.

[48] S.Z. Shmurak, V.V. Kedrov, A.P. Kiselev, T.N. Fursova, I.I. Zver'kova, S.S. Khasanov, Spectral and structural characteristics of molybdates $(Lu_{1-x}Eu_x)_2$ $(MoO_4)_3$, Phys. Solid State 61 (2019) 632–641, https://doi.org/10.1134/S1063783419040280.

[49] B. Wang, X. Li, Q. Zeng, G. Yang, J. Luo, X. He, Y. Chen, Efficiently enhanced photoluminescence in Eu^{3+}-doped $Lu_2(MoO_4)_3$ by Gd^{3+} substituting, Mater. Res. Bull. 100 (2018) 97–101, https://doi.org/10.1016/j.materresbull.2017.12.004.

[50] M.H. Chokayri, L. Rabardel, B. Elouadi, Investigation par analyse thermique différentielle du système $Gd_2(MoO_4)_3$-$Bi_2(MoO_4)_3$, Thermochim. Acta 112 (1987) 245–257, https://doi.org/10.1016/0040-6031(87)88281-3.

[51] B. Joukoff, G. Grimouille, G. Leroux, C. Daguet, A.M. Pougnet, Crystal growth and crystallographic data of some $Ln_2(MoO_4)_3$ type mixed rare earth molybdates, J. Cryst. Growth 46 (1979) 445–450, https://doi.org/10.1016/0022-0248(79)90094-0.

[52] Z. Lin, X. Han, C. Zaldo, Solid state reaction synthesis and optical spectroscopy of ferroelectric $(Gd_{1-x}Ln_x)_2(MoO_4)_3$; with Ln=Yb or Tm, J. Alloys Compd. 492 (2010) 77–82, https://doi.org/10.1016/j.jallcom.2009.11.094.

[53] M. Zhang, C. Cao, X. Chen, Z. Chen, L. Yang, Y. Li, A. Xie, Synthesis, luminescent properties, and thermal stabilities of $Gd_{2(1-x)}Eu_{2x}(Mo_yW_{1-y}O_4)_3$ ($0 \leq x \leq 0.2$, $0 \leq y \leq 1$) solid solution phosphors, Solid State Sci. 120 (2021), 106710, https://doi.org/10.1016/j.solidstatesciences.2021.106710.

[54] Nanci Prado Sabalisck, Gerardo Gil-de-Cos, Cristina González-Silgo, Candelaria Guzmán-Afonso, Víctor Lavín Javier López-Solano, Isabel Teresa Martín-Mateos, Lourdes Mestres, Andrés Mujica, David Santamaría-Pérez, Manuel Eulalio Torres y Xavier Vendrel, Role of rare earth sites and vacancies in the anomalous compression of modulated scheelite tungstates $RE_2(WO_4)_3$, Phys. Rev. Mater. 5 (2021), 123601, https://doi.org/10.1103/PhysRevMaterials.5.123601.

[55] B. Elouadi, S. Kholtei, M.H. Chokayri, M. Drache, J.C. Boivin, Stability and phase transitions in rare earth molybdates crystallizing with β-$Gd_2(MoO_4)_3$ structure, Ferroelectrics 108 (1990) 195–200, https://doi.org/10.1080/00150199008018756.

[56] A. Hernández-Suárez, C. Guzmán-Afonso, J. López-Solano, C. González-Silgo, M.E. Torres, N. Sabalisck, E. Matesanz, J. Rodríguez-Carvajal, Ferroic phase transition in $LaEr(MoO_4)_3$, Powder Diffr. 28 (2013) S86–S93, https://doi.org/10.1017/S0885715613001127.

[57] D.M. Bubb, D. Cohen, S.B. Qadri, Infrared-to-visible upconversion in thin films of $LaEr(MoO_4)_3$, Appl. Phys. Lett. 87 (2005), 131909, https://doi.org/10.1063/1.2067712.

[58] U. Gurudas, D.M. Bubb, Nonlinear optical characterization of $LaEr(MoO_4)_3$ thin films using the Z-scan technique, Appl. Phys. A 88 (2007) 255–259, https://doi.org/10.1007/s00339-007-4019-4.

[59] A. Khare, A critical review on the efficiency improvement of upconversion assisted solar cells, J. Alloys Compd. 821 (2020), 153214, https://doi.org/10.1016/j.jallcom.2019.153214.

[60] Universidad de La Laguna, Servicio general de Apoyo a la Investigación (SEGAI), servicio de Integrado de Difracción de Rayos X. https://www.ull.es/servicios/segai/servicios/difraccion-rx/.

[61] Universidad de La Laguna, Servicio general de Apoyo a la Investigación (SEGAI). Servicio de Análisis térmico. https://www.ull.es/servicios/segai/servicios/analisis-termico/.

[62] Radiant Tecnologies, Inc.®, Radiant Precisión Series with Visión Software Hardware Architecture and System Desing, 2008. Radiant Tecnologies, https://www.ferrodevices.com/1/297/lc.asp.

[63] J. Rodríguez-Carvajal, Commission on powder diffraction (IUCr), Newsletter 26 (2001) 12–19, http://journals.iucr.org/iucr-top/comm/cpd/Newsletters/). The complete program and documentation can be obtained in http://www.ill.eu/sites/fullprof/.

[64] D. Orobengoa, C. Capillas, M.I. Aroyo, J.M. Perez-Mato, AMPLIMODES: symmetry-mode analysis on the Bilbao crystallographic server, J. Appl. Crystallogr. 42 (2009) 820–833, https://doi.org/10.1107/S0021889809028064.

[65] J. Park, B.G. Kim, S. Mori, T. Oguchi, Tetrahedral tilting and ferroelectricity in Bi_2AO_5 (A = Si, Ge) from first principles calculations, J. Solid State Chem. 235 (2016) 68–75, https://doi.org/10.1016/j.jssc.2015.12.011.

[66] C. Capillas, E.S. Tasci, G. de la Flor, D. Orobengoa, J.M. Perez-Mato, M.I. Aroyo, A new computer tool at the Bilbao Crystallographic Server to detect and characterize pseudosymmetry, Z. Kristallogr. 226 (2011) 186–196, https://doi.org/10.1524/zkri.2011.1321.

[67] D.A. Cardwell, D.S. Ginley, Handbook of Superconducting Materials: Superconductivity, Materials and Processes, first ed., CRC Press, Boca Raton, 2002 https://doi.org/10.1201/9781420034202.

[68] Lorraine F. Francis, Materials Processing: A Unified Approach to Processing of Metals, Ceramics and Polymers, Prentice Hall, Englewood Cliffs, 1999, in: https://www.sciencedirect.com/book/9780123851321/materials-processing.

[69] A.K. Galwey, M.E. Brown, Thermal Decomposition of Ionic Solids, Elsevier, Amsterdam, 1999. https://www.sciencedirect.com/bookseries/studies-in-physical-and-theoretical-chemistry/vol/86/suppl/C.

[70] I. Bhat, S. Husain, W. Khan, S.I. Patil, Effect of Zn doping on structural, magnetic and dielectric properties of $LaFeO_3$ synthesized through sol–gel auto-combustion process, Mater. Res. Bull. 48 (2013) 4506–4512, https://doi.org/10.1016/j.materresbull.2013.07.028.

[71] S. Bdey, N.F. Bourguiba, S.N. Savvin, P. Nuñez, $Na_3Bi(AsO_4)_2$: synthesis, crystal structure and ionic conductivity, J. Solid State Chem. 272 (2019) 189–197, https://doi.org/10.1016/j.jssc.2019.01.034.

[72] A.K. Jonscher, Dielectric relaxation in solids, J. Phys. D Appl. Phys. 32 (1999) R57, https://doi.org/10.1088/0022-3727/32/14/201.

[73] C. Guzmán-Afonso, M.E. Torres, C. González-Silgo, N. Sabalisck, J. González-Platas, E. Matesanz, A. Mujica, Electrical transport and anomalous structural behavior of α-$Eu_2(MoO_4)_3$ at high temperature, Solid State Commun. 151 (2011) 1654–1658, https://doi.org/10.1016/j.ssc.2011.08.009.

[74] I.D. Brown, The Chemical Bond in Inorganic Chemistry: the Bond Valence Model, 27, Oxford University Press, 2016, https://doi.org/10.1093/acprof:oso/9780199298815.001.0001.

[75] M. Xu, Y. Yu, H. Zhang, J. Wangi, Growth and characterization of ferroelectric Tb2(MoO4)3 crystal, J. Rare Earths 27 (2) (2009) 192, https://doi.org/10.1016/S1002-0721(08)60218-5.

[76] J. F. Scott. Ferroelectrics go bananas. J. Phys. Condens. Matter 20 021001. https://doi.org/10.1088/0953-8984/20/02/021001.

[77] P. Barrozo, D.R. Småbråten, Y.-L. Tang, B. Prasad, S. Saremi, R. Ozgur, V. Thakare, R.A. Steinhardt, M.E. Holtz, V.A. Stoica, L.W. Martin, D.G. Schlom, S.M. Selbach, R. Ramesh, Defect-enhanced polarization switching in the improper ferroelectric $LuFeO_3$, Adv. Mater. 32 (2020), 2000508, https://doi.org/10.1002/adma.202000508.

[78] C. González-Silgo, M.E. Torres, N.P. Sabalisck, I.T. Martín-Mateos, E. Zanardi, A. Mujica, F. Lahoz, J. López-Solano, C. Guzmán-Afonso, in: A. Laref (Ed.), Polarons: Recent Progress and Perpectives, Nova Science, 2018. https://novapublishers.com/shop/polarons-recent-progress-and-perspectives/.

[79] K. Nassau, H.J. Levinstein, G.M. Loiacono, A comprehensive study of trivalent tungstates and molybdates of the type $L_2(MO_4)_3$, J. Phys. Chem. Solid. 26 (1965) 1805–1816, https://doi.org/10.1016/0022-3697(65)90213-1.

[80] I.R. Martin, F. Lahoz, V. Lavin, M. Hernandez-Molina, Optical properties of Eu^{3+} in malonate crystals to monitor a structural phase transition, Opt. Mater. 25 (2004) 223–229, https://doi.org/10.1117/12.525861.

[81] F. Paz-Buclatin, S. Ríos, I.R. Martín, L.L. Martin, Fluorescence intensity ratio and whispering gallery mode techniques in optical temperature sensors: comparative study, Opt. Mater. Express 9 (2019) 4126–4137, https://doi.org/10.1364/OME.9.004126.

[82] T.V. Gavrilović, D.J. Jovanović, V.M. Lojpur, V. Đorđević, M.D. Dramićanin, Enhancement of luminiscence emission from $GdVO_4$: Er^{3+}/Yb^{3+} phosphor by Li^+ co-doping, J. Solid State Chem. 217 (2014) 92–98, https://doi.org/10.1016/j.jssc.2014.05.009.